JOURNAL OF COMPUTATIONAL PHYSICS **123,** 1–14 (1996)
ARTICLE NO. 0001

Extension of the Piecewise Parabolic Method to One-Dimensional Relativistic Hydrodynamics

JOSÉ Mª MARTÍ* AND EWALD MÜLLER

Max-Planck-Institut für Astrophysik, Karl-Schwarzschild-Str. 1, 85740 Garching, Germany

Received July 25, 1994; revised April 28, 1995

An extension to 1D relativistic hydrodynamics of the piecewise parabolic method (PPM) of Colella and Woodward using an exact relativistic Riemann solver is presented. Results of several tests involving ultrarelativistic flows, strong shocks and interacting discontinuities are shown. A comparison with Godunov's method demonstrates that the main features of PPM are retained in our relativistic version. © 1996 Academic Press, Inc.

1. INTRODUCTION

Relativistic hydrodynamics (RHD here after) plays an important role in different fields of physics, e.g., in astrophysics, cosmology, and nuclear physics. In extragalactic jets emanating from core dominated radio sources associated with active galactic nuclei [1] or in current laboratory heavy-ion reactions [2] even ultrarelativistic flows are encountered. The necessity of modeling such relativistic flows which also involve strong shocks is triggering the development of relativistic hydro-codes.

The first code to solve the RHD equations on an Eulerian grid was developed by Wilson [3, 4] and collaborators [5, 6]. The code is based on explicit finite differencing techniques and uses a monotonic transport algorithm to discretize the advection terms of the RHD equations. The stabilization of the code across shocks is accomplished by means of a von Neumann and Richtmyer [7] artificial viscosity. This code has been widely used in numerical cosmology, axisymmetric relativistic stellar collapse, accretion onto compact objects, and, more recently, in collisions of heavy ions. The code's acccuracy decreases as the flow becomes strongly relativistic (flow Lorentz factor, $W > 2$; see [5]).

Norman and Winkler [8] proposed a fully implicit treatment of the equations in order to overcome the numerical problems in the ultrarelativistic limit ($W \gg 1$). Recently, several new methods for numerical RHD have appeared [9–15] which with the exception of [11] (smoothed particle hydrodynamics) and [10] (flux-corrected transport method for the equations of relativistic magnetohydrodynamics) are based on the *conservation form* of the RHD equations. One advantage of this approach is the possibility of using numerical techniques specially designed to solve nonlinear hyperbolic systems of conservation laws [9]. In fact, the codes described in Refs. [9, 12, 15] and the code HLLE of [14] are based on Godunov-type methods and an implementation of different approximate Riemann solvers (readers lacking knowledge of Godunov-type methods and Riemann solvers should consult, e.g., the recent book of LeVeque [16]). Judging from the results of several test calculations shown in these references, it can be concluded that an accurate description of ultrarelativistic flows with strong shock waves can be accomplished by writing the system of RHD in conservation form and using Riemann solvers.

In a recent paper [17] we have derived the exact solution of the Riemann problem for ideal gases in relativistic hydrodynamics. Similarly to the classical (Newtonian) case, the solution can be obtained by solving an implicit algebraic equation which determines the pressure in the intermediate states that develop after breakup of the initial discontinuity. Our solution extends previously known particular solutions (i.e., [18, 19]) to the general case of two arbitrary initial states. It can be used to construct an exact Riemann solver and allows one to formulate a relativistic version of Godunov's method.

On the other hand, the piecewise parabolic method ([20], PPM hereafter), is a well-known higher-order extension of Godunov's method being used extensively in classical hydrodynamics. Besides the use of an exact Riemann solver, the key ingredients responsible for the accuracy of PPM are a parabolic interpolation of variables inside numerical cells and special monotonicity constraints and discontinuity steepeners to keep discontinuities sharp and free of numerical oscillations. Finally, solving Riemann problems for states averaged over the domain of dependence of the interfaces makes PPM second-order accurate in time. In this paper, we present an extension of PPM in its direct Eulerian version to one-dimensional RHD, in which all the key ingredients of PPM have properly been generalized.

The paper is organized as follows. In Section 2 we define the RHD equations in an Eulerian reference frame in conservation form and describe the transformation of quantities from the Eulerian frame to the rest (proper) frame of a fluid element.

* Present address: Departamento de Astronomía y Astrofísica, Universidad de Valencia, 46100 Burjassot, Valencia, Spain.

0021-9991/96 $12.00

This transformation is a key ingredient in our algorithm. Section 3 is devoted to a description of the reconstruction procedure, the determination of effective second-order-accurate (in time) left and right states defining the Riemann problems and the calculation of the numerical fluxes using an exact relativistic Riemann solver. Several numerical test calculations including the RHD generalization of the interaction of two blast waves [22] are presented in Section 4. In Appendix I, the explicit formulae used in the interpolation step are given. Finally, the analytical solution corresponding to the problem of the interaction of two relativistic blast waves introduced in Section 4 is described in Appendix II.

2. THE EQUATIONS OF RELATIVISTIC HYDRODYNAMICS

In an Eulerian reference frame, the equations of RHD of a perfect fluid in one spatial (Cartesian) coordinate x can be written in conservation form as

$$\frac{\partial D}{\partial t} + \frac{\partial Dv}{\partial x} = 0 \tag{1}$$

$$\frac{\partial S}{\partial t} + \frac{\partial (Sv + p)}{\partial x} = 0 \tag{2}$$

$$\frac{\partial \tau}{\partial t} + \frac{\partial (S - Dv)}{\partial x} = 0, \tag{3}$$

where D, S, and τ are the rest-mass density, the momentum density, and the energy density in a fixed frame, respectively. These variables are related to quantities in the local rest frame of the fluid through

$$D = \rho W \tag{4}$$

$$S = \rho h W^2 v \tag{5}$$

$$\tau = \rho h W^2 - p - D, \tag{6}$$

where ρ, p, v, W, and h are the proper rest-mass density, the pressure, the fluid velocity, the fluid Lorentz factor, and the specific enthalpy, respectively. The latter two quantities are given by

$$W = \frac{1}{\sqrt{1 - v^2}} \tag{7}$$

and

$$h = 1 + \varepsilon + \frac{p}{\rho}, \tag{8}$$

where ε is the specific internal energy. Note that in the previous equations and throughout the whole paper the speed of light is set equal to unity.

From Eqs. (4)–(6) the following relation between p, v, and the conserved quantities can easily be derived:

$$v = \frac{S}{\tau + D + p}. \tag{9}$$

In the non-relativistic limit ($v \to 0$, $h \to 1$) D, S, and τ approach their Newtonian counterparts, ρ, ρv, and $\rho E = \rho\varepsilon + \rho v^2/2$, and Eqs. (1)–(3) reduce to the classical ones,

$$\frac{\partial \rho}{\partial t} + \frac{\partial \rho v}{\partial x} = 0 \tag{10}$$

$$\frac{\partial \rho v}{\partial t} + \frac{\partial (\rho v^2 + p)}{\partial x} = 0 \tag{11}$$

$$\frac{\partial \rho E}{\partial t} + \frac{\partial v(\rho E + p)}{\partial x} = 0. \tag{12}$$

The system of Eqs. (1)–(3) with definitions (4)–(8) is closed by means of an equation of state (EOS), which we shall assume as given in the form

$$p = p(\rho, \varepsilon). \tag{13}$$

In order to use the exact solution of the relativistic Riemann problem derived in [17] we restrict ourselves to an ideal gas EOS, i.e.,

$$p = (\gamma - 1)\rho\varepsilon, \tag{14}$$

where γ is the adiabatic index. A very important quantity derived from the EOS is the local sound velocity c, which in our case is defined through

$$c^2 = \frac{\gamma p}{\rho h}. \tag{15}$$

In any RHD code evolving the conserved quantities $\{D, S, \tau\}$ in time, the variables $\{p, \rho, \varepsilon, v\}$ have to be computed from the conserved quantities at least once per time step. In our approach, like in Refs. [9, 12], this is achieved using relations (4)–(8) and (14) to construct the function

$$f(p) = (\gamma - 1)\rho_* \varepsilon_* - p \tag{16}$$

with ρ_* and ε_* given by

$$\rho_* = \frac{D}{W_*} \tag{17}$$

and

$$\varepsilon_* = \frac{\tau + D(1 - W_*) + p(1 - W_*^2)}{DW_*}, \tag{18}$$

respective, where

$$W_* = \frac{1}{\sqrt{1 - (S/(\tau + D + p))^2}}. \tag{19}$$

The zero of $f(p)$ in the physically allowed domain $p \in]p_{\min}, \infty[$ determines the pressure, the monotonicity of $f(p)$ in that domain ensuring the uniqueness of the solution. The lower bound of the physically allowed domain, $p_{\min}$, defined by

$$p_{\min} = |S| - \tau - D, \tag{20}$$

is obtained from (9) by taking into account that (in our units) $|v| \leq 1$. Knowing p, Eq. (9) then directly gives v, while the remaining state quantities are straightforwardly obtained from Eqs. (4)–(8).

3. A RELATIVISTIC VERSION OF PPM

Equations (1)–(3) can be written in the form

$$\frac{\partial \mathbf{u}}{\partial t} + \frac{\partial \mathbf{F}(\mathbf{u})}{\partial x} = 0 \tag{21}$$

with

$$\mathbf{u} = (D, S, \tau)^{\mathrm{T}} \tag{22}$$

and

$$\mathbf{F} = (Dv, Sv + p, S - Dv)^{\mathrm{T}}. \tag{23}$$

In order to solve system (21) we consider the conservative difference scheme

$$\mathbf{u}_j^{n+1} = \mathbf{u}_j^n + \frac{\Delta t}{\Delta x}\{\hat{\mathbf{F}}_{j-1/2} - \hat{\mathbf{F}}_{j+1/2}\}, \tag{24}$$

where $\mathbf{u}_j^n$ and $\mathbf{u}_j^{n+1}$ are the zone-averaged values of the state vector $\mathbf{u}$ of zone j at times $t = t^n$ and $t = t^{n+1} = t^n + \Delta t$, respectively. $\hat{\mathbf{F}}_{j\pm1/2}$ are the time-averaged numerical fluxes at the right and left interfaces of zone j. In a Godunov-type difference scheme appropriate left and right states are constructed from the zone-averaged values, which are then used to calculate the numerical fluxes $\hat{\mathbf{F}}_{j+1/2}$ by solving the corresponding Riemann problem.

In the remainder of this section we discuss in detail how the numerical fluxes are calculated in our relativistic version of PPM. First, we describe the interpolation procedure used to reconstruct the variables inside zones from zone-averaged values. Then, we concentrate on the construction of left and right interface states averaged over the domain of dependence of each interface, which are used as initial states for the Riemann problem to be solved at each interface. Finally, we discuss the solution of the relativistic Riemann problem and the computation of the numerical fluxes.

3.1. *Interpolation Procedure*

In our relativistic version of PPM the interpolation algorithm described in the original paper by Colella and Woodward [20] is applied to zone-averaged values of $\mathbf{V} = (p, \rho, v)$, which are obtained from zone averaged values of the conserved quantities $\mathbf{u}_j$.

Interpolating in $\mathbf{V}$ instead of, for example, in $\mathbf{u}$ has several advantages. First, in this case the solution of Eq. (16), which involves an iteration, has to be computed only once per zone per time step, and second, one can easily avoid the occurrence of unphysical values (i.e., larger than the speed of light) for the interpolated flow velocity. Third, interpolating in p and ρ simplifies the implementation of the contact discontinuity detector (see Appendix I).

Like in the Newtonian version of PPM, we determine for each zone j the quartic polynomial which has zone-averaged values $a_{j-2}, a_{j-1}, a_j, a_{j+1}, a_{j+2}$ to interpolate the structure inside the zone, where a is one of the quantities p, ρ, or v. Using this quartic polynomial values of a at the left and right interfaces of the zones, $a_{L,j}$ and $a_{R,j}$, are obtained. These reconstructed values are then modified such that the parabolic profile, which is uniquely determined by $a_{L,j}$, $a_{R,j}$, and a_j, is monotonic inside the zone (monotonization). Finally, the interpolation procedure is slightly modified near discontinuities to produce narrower jumps (see Appendix I).

3.2. *Construction of Effective Left and Right States*

To obtain time-averaged fluxes at an interface $j + \frac{1}{2}$ separating zones j and $j + 1$, in PPM two spatially averaged states, $\mathbf{V}_{j+1/2,S}$ ($S = L, R$, where L and R denote the left and right sides of the interface, respectively), are constructed, which take into account the characteristic information reaching the interface from both sides during the time step.

In the Lagrangian version of PPM this implies to calculate the average of $\mathbf{V}$ over the domain of dependence of each interface. In its direct Eulerian version, however, the construction of the effective states is more complicated, because the number of characteristics reaching the interface of a zone from a given side can vary from zero to three. In a first step, one computes the average over that part of the domain of dependence of each interface, which lies to the left and right of the interface. The initial guess is then corrected by subtracting that amount of each characteristic which will not reach the interface during the time step (see Fig. 5 in [20]).

In our relativistic version of PPM the correction of the initial guess is obtained by closely following the procedure in [20], but

TABLE I

Spectral Decomposition of Matrix **A**

Eigenvalues	Left eigenvectors	Right eigenvectors
$\lambda_- = \frac{v-c}{1-vc}$	$\mathbf{l}_- = \left(0, \frac{1}{2}, -\frac{1}{2\rho h W^2 c}\right)$	$\mathbf{r}_- = \left(-\frac{\rho W^2}{c}, 1, -\rho h W^2 c\right)$
$\lambda_0 = v$	$\mathbf{l}_0 = \left(1, 0, -\frac{1}{hc^2}\right)$	$\mathbf{r}_0 = (1, 0, 0)$
$\lambda_+ = \frac{v+c}{1+vc}$	$\mathbf{l}_+ = \left(0, \frac{1}{2}, \frac{1}{2\rho h W^2 c}\right)$	$\mathbf{r}_+ = \left(\frac{\rho W^2}{c}, 1, \rho h W^2 c\right)$

Note. Left and right eigenvectors have been chosen such that $\mathbf{l}_\# \cdot \mathbf{r}_{\#'} = \delta_{\#\#'}$; $\#, \#' = -, 0, +$.

considering the characteristic speeds and Riemann invariants of the equations of relativistic instead of Newtonian hydrodynamics. We rewrite system (21) in terms of $\mathbf{V}$ in characteristic form as

$$\frac{\partial \mathbf{V}}{\partial t} + \mathbf{A}\frac{\partial \mathbf{V}}{\partial x} = 0, \tag{25}$$

where matrix $\mathbf{A}$ is defined as

$$\mathbf{A} = \begin{pmatrix} v & \frac{\rho}{1-v^2c^2} & \frac{-v}{hW^2(1-v^2c^2)} \\ 0 & \frac{v(1-c^2)}{1-v^2c^2} & \frac{1}{\rho h W^4(1-v^2c^2)} \\ 0 & \frac{\rho h c^2}{1-v^2c^2} & \frac{v(1-c^2)}{1-v^2c^2} \end{pmatrix}. \tag{26}$$

Note that the local sound speed, c, defined in (15) has explicitly been introduced in matrix $\mathbf{A}$, whose eigenvalues $\lambda_\#$ ($\# \in \{-, 0, +\}$) and corresponding left and right eigenvectors $\mathbf{l}_\#$ and $\mathbf{r}_\#$ are given in Table I. In analogy with [20] the effective left and right states, $\mathbf{V}_{j+1/2,S}$ ($S = L, R$), are then found to be

$$p_{j+1/2,S} = \tilde{p}_{j+1/2,S} + \tilde{C}^2_{j+1/2,S}(\beta^+_{j+1/2,S} + \beta^-_{j+1/2,S}) \tag{27}$$

$$v_{j+1/2,S} = \tilde{v}_{j+1/2,S} + \tilde{C}_{j+1/2,S}(\beta^+_{j+1/2,S} - \beta^-_{j+1/2,S}) \tag{28}$$

$$\rho_{j+1/2,S} = \tilde{\rho}_{j+1/2,S} + \tilde{R}_{j+1/2,S}(\beta^+_{j+1/2,S} - \beta^0_{j+1/2,S} + \beta^-_{j+1/2,S}) \tag{29}$$

with

$$\beta^\#_{j+1/2,L} = 0 \quad \text{if } \lambda_\#(\mathbf{V}_j) \le 0 \tag{30}$$

$$\beta^\#_{j+1/2,R} = 0 \quad \text{if } \lambda_\#(\mathbf{V}_{j+1}) \ge 0 \tag{31}$$

and

$$\beta^\pm_{j+1/2,S} = \mp\frac{1}{2\tilde{C}_{j+1/2,S}}\left(\tilde{v}_{j+1/2,S} - v^\pm_{j+1/2,S} \pm \frac{\tilde{p}_{j+1/2,S} - p^\pm_{j+1/2,S}}{\tilde{C}_{j+1/2,S}}\right) \tag{32}$$

$$\beta^0_{j+1/2,S} = \frac{\tilde{p}_{j+1/2,S} - \rho^0_{j+1/2,S}}{\tilde{R}_{j+1/2,S}} - \frac{\tilde{p}_{j+1/2,S} - p^0_{j+1/2,S}}{\tilde{C}^2_{j+1/2,S}} \tag{33}$$

otherwise.

The quantities $a^\#_{j+1/2,S}$ ($S = L, R$; $a \in \{p\ \rho, v\}$) are the averages of a over that part of the domain of dependence of the #-characteristic, which lies to the left (right) of the respective interface. They are calculated using the (monotonized) parabolae determined for a in the interpolation step; i.e.,

$$a^\#_{j+1/2,L} = a_{R,j} - \frac{x}{2}\left[a_{R,j} - a_{L,j} - 6\left(1 - \frac{2}{3}x\right)\left(a_j - \frac{a_{L,j} + a_{R,j}}{2}\right)\right], \tag{34}$$

where

$$x = \frac{\max(0, \Delta t \lambda_\#(\mathbf{V}_j))}{x_{j+1/2} - x_{j-1/2}} \tag{35}$$

and

$$a^\#_{j+1/2,R} = a_{L,j+1} + \frac{x}{2}\left[a_{R,j+1} - a_{L,j+1} + 6\left(1 - \frac{2}{3}x\right)\left(a_{j+1} - \frac{a_{L,j+1} + a_{R,j+1}}{2}\right)\right], \tag{36}$$

where

$$x = \frac{\max(0, -\Delta t \lambda_\#(\mathbf{V}_{j+1}))}{x_{j+3/2} - x_{j+1/2}}. \tag{37}$$

Note that we have defined x in Eqs. (35) and (37), and hence $a^\#_{j+1/2,S}$, slightly different from Colella and Woodward ([20]; see their Eq. (3.5)). However, the resulting $\beta^\#_{j+1/2,S}$, the only quantities depending on $a^\#_{j+1/2,S}$, are identical to those of [20], because they have to fulfill Eqs. (30) and (31). With our modified definition of $a^\#_{j+1/2,S}$, the quantities $\tilde{a}_{j+1/2,S}$ appearing in Eqs. (27) to (33) are then simply given by

$$\tilde{a}_{j+1/2,L} = a^+_{j+1/2,L} \tag{38}$$

$$\tilde{a}_{j+1/2,R} = a^-_{j+1/2,R}. \tag{39}$$

Finally, the quantities $\tilde{C}_{j+1/2,S}$ and $\tilde{R}_{j+1/2,S}$ are defined according to

$$\tilde{C}_{j+1/2,S} = \tilde{\rho}_{j+1/2,S}\tilde{h}_{j+1/2,S}\tilde{W}^2_{j+1/2,S}\tilde{c}_{j+1/2,S} \tag{40}$$

$$\tilde{R}_{j+1/2,S} = \tilde{\rho}^2_{j+1/2,S}\tilde{h}_{j+1/2,S}\tilde{W}^4_{j+1/2,S} \tag{41}$$

$\tilde{h}_{j+1/2,S}$, $\tilde{W}_{j+1/2,S}$, and $\tilde{c}_{j+1/2,S}$ being given as functions of $\tilde{p}_{j+1/2,S}$, $\tilde{\rho}_{j+1/2,S}$, and $\tilde{v}_{j+1/2,S}$ (see Eqs. (8), (7), and (15), respectively).

It is worthwhile to note that the Newtonian limits of $\beta^+_{j+1/2,S}$ and $\beta^-_{j+1/2,S}$ coincide with the corresponding coefficients in Eq. (3.7) of [20]. However, the limit of $\beta^0_{j+1/2,S}$ differs from its Newtonian counterpart, because contrary to [20] we have used the density instead of the specific volume as a variable for the characteristic equations.

3.3. *Solution of the Riemann Problem and Computation of the Numerical Fluxes*

In Godunov's approach the numerical fluxes $\hat{\mathbf{F}}_{j+1/2}$ are calculated according to

$$\hat{\mathbf{F}}_{j+1/2} = \mathbf{F}(\overline{\mathbf{u}}_{j+1/2}), \tag{42}$$

where $\overline{\mathbf{u}}_{j+1/2}$ is an approximation to $(1/\Delta t)\int \mathbf{u}(x_{j+1/2}, t)\, dt$, i.e., the time-averaged value of the solution at $x_{j+1/2}$, which is obtained solving the Riemann problem at $x_{j+1/2}$ with left and right states $\mathbf{V}_{j+1/2,L}$ and $\mathbf{V}_{j+1/2,R}$, respectively.

In a recent paper [17] we have shown that an exact solution of a Riemann problem for a polytropic gas in RHD can be obtained, in complete analogy to the Newtonian case, by solving a non-linear algebraic equation.

Both in relativistic and Newtonian hydrodynamics the discontinuity between the two constant initial states $\mathbf{V}_L$ and $\mathbf{V}_R$ decays into two elementary nonlinear waves (shocks or rarefactions), one moving towards the initial left state and the other towards the initial right state. Between the waves two new states $\mathbf{V}_{L*}$ and $\mathbf{V}_{R*}$ appear, which are separated from each other through a contact discontinuity moving along with the fluid. Across the contact discontinuity, pressure and velocity are continuous, while the density exhibits a jump. As in classical hydrodynamics [24] the self-similar character of the flow through rarefaction waves and the Rankine–Hugoniot conditions across shocks provide the conditions to link the intermediate states $\mathbf{V}_{S*}$ ($S = L, R$) with their corresponding initial state $\mathbf{V}_S$. In particular, one can express the velocity of the intermediate states v_{S*} as a function of the pressure p_{S*} of these states. The smoothness of the velocity across the contact discontinuity then gives

$$v_{L*}(p_*) = v_{R*}(p_*), \tag{43}$$

where $p_* = p_{L*} = p_{R*}$. This is the above mentioned non-linear algebraic equation to be solved at each interface in each time step. The functions $v_{S*}(p)$ are defined by

$$v_{S*}(p) = \begin{cases} \mathcal{R}^S(p) & \text{if } p \le p_S \\ \mathcal{S}^S(p) & \text{if } p > p_S, \end{cases} \tag{44}$$

where $\mathcal{R}^S(p)$ ($\mathcal{S}^S(p)$) denotes the family of all states which can be connected through a rarefaction (shock) with a given state S ahead of the wave (for more details see [17]). Because the Riemann invariants

$$J_\pm = \frac{1}{2}\ln\left(\frac{1+v}{1-v}\right) \pm \int \frac{c}{\rho}\, d\rho \tag{45}$$

are constant through rarefaction waves propagating to the left (J_+) or right (J_-), one can derive

the expression

$$\mathcal{R}^S(p) = \frac{(1+v_S)A_\pm(p) - (1-v_S)}{(1+v_S)A_\pm(p) + (1-v_S)} \tag{46}$$

with

$$A_\pm(p) = \left(\frac{\sqrt{\gamma-1} - c(p)}{\sqrt{\gamma-1} + c(p)}\,\frac{\sqrt{\gamma-1} + c_S}{\sqrt{\gamma-1} - c_s}\right)^{\pm 2/\sqrt{\gamma-1}} \tag{47}$$

the $+$ ($-$) sign of $A_\pm$ corresponding to $S = L$ ($S = R$). In Eq. (47), c_S is the sound speed of the state S, and $c(p)$ is given by

$$c(p) = \left(\frac{\gamma(\gamma-1)p}{(\gamma-1)\rho_S(p/p_S)^{1/\gamma} + \gamma p}\right)^{1/2}. \tag{48}$$

The family of all states $\mathcal{S}^S(p)$, which can be connected through a shock with a given state S ahead of the wave, is determined by the shock jump conditions. One obtains (see [17])

$$\mathcal{S}^S(p) = \left(h_S W_S v_S \pm \frac{p - p_S}{j(p)\sqrt{1 - V_\pm(p)^2}}\right) \left[h_S W_S + (p - p_S)\left(\frac{1}{\rho_S W_S} \pm \frac{v_S}{j(p)\sqrt{1 - V_\pm(p)^2}}\right)\right]^{-1}, \tag{49}$$

where the $+$ ($-$) sign corresponds to $S = R$ ($S = L$). $V_\pm(p)$ and $j(p)$ denote the shock velocity and the modulus of the mass flux across the shock front, respectively. They are given by

$$V_\pm(p) = \frac{\rho_S^2 W_S^2 v_S \pm j(p)^2\sqrt{1 + (\rho_S/j(p))^2}}{\rho_S^2 W_S^2 + j(p)^2} \tag{50}$$

and

$$j(p) = \sqrt{(p_S - p)\Big/\left(\frac{h_S^2 - h(p)^2}{p_S - p} - \frac{2h_S}{\rho_S}\right)}, \tag{51}$$

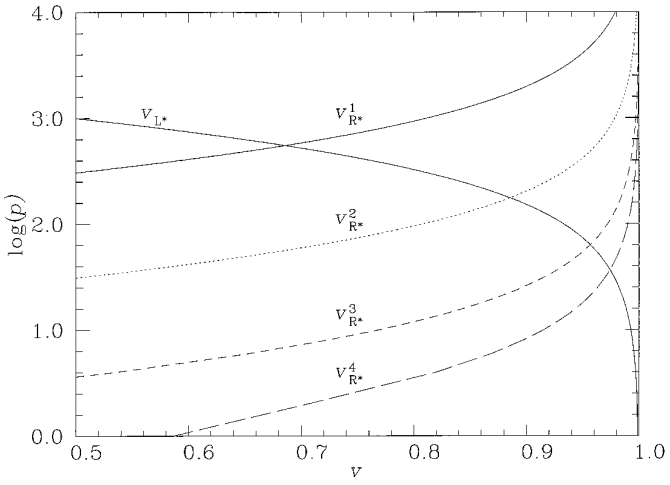

FIG. 1. Graphical solution in the p-v plane of the Riemann problems defined by the initial states $\mathbf{V}_L = (p_L = 10^3,\ \rho_L = 1,\ v_L = 0.5)$ and $\mathbf{V}^i_R = (p^i_R,\ \rho_R = 1,\ v_R = 0)$ $(i = 1, ..., 4)$ with $p^1_R = 10^2$, $p^2_R = 10$, $p^3_R = 1$, $p^4_R = 10^{-1}$. The adiabatic index of the equation of state is $\frac{5}{3}$ in all cases. Note the asymptotic behaviour of the functions when they approach $v = 1$.

where the enthalpy $h(p)$ of the state behind the shock is the (unique) positive root of the quadractic equation

$$h^2\left(1 + \frac{(\gamma-1)(p_S - p)}{\gamma p}\right) - \frac{(\gamma-1)(p_S - p)}{\gamma p} \\ h + \frac{h_S(p_S - p)}{\rho_S} - h_S^2 = 0, \tag{52}$$

which is obtained from the Taub adiabat (the relativistic version of the Hugoniot adiabat) for an ideal gas equation of state.

In Fig. 1, the functions $v_{L_*}(p)$ and $v_{R_*}(p)$ are displayed in a p-v diagram for a particular set of Riemann problems. In the calculations presented here, Eq. (43) is solved for the pressure p_* of the intermediate states by a combination of interval bisection and quadratic interpolation following the procedure described in [25]. Once p_* has been obtained, the remaining state quantities can easily be derived [17].

Now we are ready to determine the Riemann solution at a given interface following a procedure analogous to [26]. Let $\chi = -\text{sign}(v_*)$, where $v_* \equiv v_{L*}(p_*) = v_{R*}(p_*)$, and set

$$S = \begin{cases} L & \text{if } \chi = -1 \\ R & \text{otherwise.} \end{cases} \tag{53}$$

Then, we define

$$\tilde{\lambda}_S = \begin{cases} \dfrac{\chi v_s + c_S}{1 + \chi v_S c_S} & \text{if } p_* \le p_S \\ \chi V(p_* & \text{if } p_* > p_S \end{cases} \tag{54}$$

and

$$\tilde{\lambda}_{S*} = \begin{cases} \dfrac{\chi v_{S*} + c_{S*}}{1 + \chi v_{S*} c_{S*}} & \text{if } p_* \le p_S \\ \chi V(p_*) & \text{if } p_* > p_S, \end{cases} \tag{55}$$

where $V(p_*)$ is the velocity of the shock (see Eq. (50)) separating states $\mathbf{V}_S$ and $\mathbf{V}_{S*}$. Note that $\tilde{\lambda}_S \ge \tilde{\lambda}_{S*}$. Hence, for $\tilde{\lambda}_{S*} \ge 0$ or $\tilde{\lambda}_S \le 0$, i.e., outside rarefaction waves, the solution of the Riemann problem at a given interface is given by

$$\bar{\mathbf{V}} = \begin{cases} \mathbf{V}_{S*} & \text{if } \tilde{\lambda}_{S*} \ge 0 \\ \mathbf{V}_S & \text{if } \tilde{\lambda}_S \le 0. \end{cases} \tag{56}$$

If $\tilde{\lambda}_S > 0 > \tilde{\lambda}_{S*}$ holds at an interface, the solution $\bar{\mathbf{V}}$ has to be evaluated inside a rarefaction wave (see [17]). In [22] the solution inside the rarefaction wave is obtained by interpolating linearly between the states on both sides of the wave, which is sufficiently accurate for Newtonian problems. However, in our relativistic variant of PPM we compute the exact solution.

Finally, the numerical fluxes at each interface are obtained according to Eq. (42). This concludes the description of our method, which is of second-order accuracy in space and time. It can be degraded to a first-order Godunov method by simply setting $a_{L,j} = a_{R,j} = a_j$ $(a = p, \rho, v)$ in the interpolation step.

4. NUMERICAL TESTS

Traditionally, numerical methods for RHD have been tested against two kinds of problems, namely wall shocks and shock tubes, giving rise to flows with large Lorentz factors and strong shock waves. Thus, we have simulated these problems with our relativistic version of PPM, too. In addition, we have calculated the more challenging problem of the interaction of discontinuities, i.e., the relativistic version of the collision of two blast waves proposed by Woodward and Colella [22].

4.1. *Shock Heating of a Cold Fluid*

The initial setup consists of an inflowing cold (i.e., $\varepsilon = 0$) gas with coordinate velocity v_1 and Lorentz factor W_1, which fills the computational grid and hits a wall placed at the opposite edge of the grid. As the gas hits the wall, it is compressed and heated up, converting its momentum into internal energy and giving rise to a shock, which starts to propagate off the wall. Behind the shock, the gas is at rest ($v_2 = 0$) and has a specific internal energy

$$\varepsilon_2 = W_1 - 1. \tag{57}$$

The compression ratio between shocked and unshocked gas, $\eta = \rho_2/\rho_1$, follows from

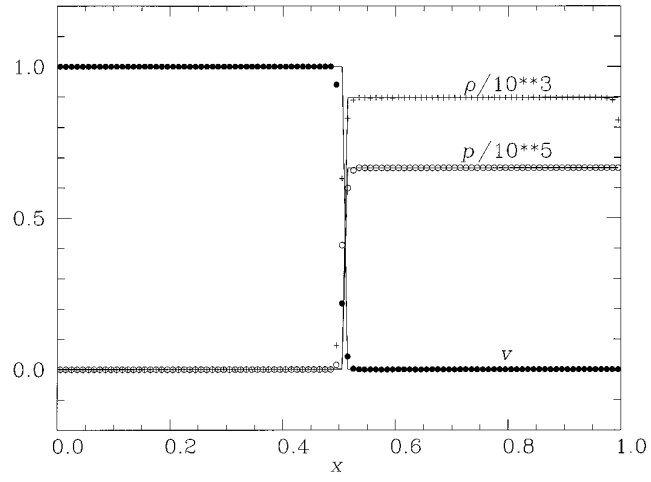

FIG. 2. Exact (solid line) and numerical profiles of pressure, density, and flow velocity for the shock heating problem with an inflow velocity $v_1 = 0.99999$, when the shock has propagated 50 zones off the wall (at $x = 1$). The computations were performed on an equidistant grid of 100 zones.

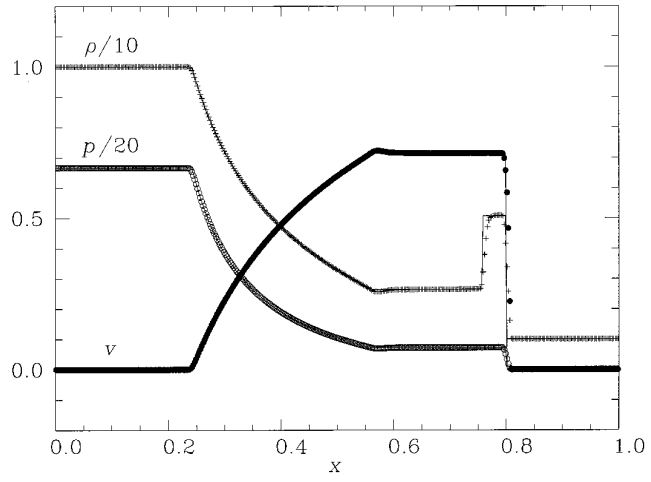

FIG. 3. Exact (solid line) and numerical profiles of pressure, density, and flow velocity of a relativistic shock tube (Problem 1; see text). The computations were performed on an equidistant grid of 400 zones.

$$\eta = \frac{\gamma + 1}{\gamma - 1} + \frac{\gamma}{\gamma - 1}\varepsilon_2, \tag{58}$$

where γ is the adiabatic index of the equation of state.

This test problem, which sometimes is also formulated as the collision of two identical gases moving at equal speed in opposite directions in order to avoid reflecting boundary conditions, has widely been used to check the accuracy of RHD codes [5, 8, 9, 12, 14, 15, 27]. Concerning explicit schemes, the numerical results improved significantly for this test problem, when numerical methods based on Riemann solvers were introduced.

In our test calculations we have used a gas with an adiabatic index $\gamma = \frac{4}{3}$ and inflow velocities ranging from nearly Newtonian to ultrarelativistic values. The computational grid consisted of 100 equidistant zones covering the interval $x \in [0, 1]$. The wall was placed at $x = 1$. For numerical reasons, the specific internal energy of the inflowing gas was set to a small finite value ($\varepsilon_1 = 10^{-7} W_1$). Figure 2 shows the profiles of pressure, rest-mass density and flow velocity for a run with a gas inflow velocity $v_1 = 0.99999$ after the shock has propagated 50 zones off the wall. The profiles obtained for other inflow velocities are qualitatively similar. The mean and maximum errors obtained for the compression ratio η are displayed in Table II for a set of inflow velocities. It shows that with our relativistic PPM the mean relative error $\bar{\varepsilon}_r(\eta)$ never exceeds a value of 10^{-3} and that, in accordance with other codes based on a Riemann solver, the accuracy of our results does not exhibit any significant dependence on the Lorentz factor of the inflowing gas.

TABLE II

Shock Heating of a Cold Gas Moving with a Velocity v_1 and a Lorentz Factor W_1

v_1	W_1	η	$\varepsilon_r^{\max}(\eta)$	$\bar{\varepsilon}_r(\eta)$
0.5	1.15	7.6188	4.3E − 02	<1.3E − 04
0.9	2.29	12.1766	5.6E − 02	6.4E − 04
0.99	7.09	31.3552	6.9E − 02	3.9E − 04
0.999	22.4	92.4651	7.5E − 02	8.6E − 04
0.9999	70.7	285.8498	7.6E − 02	5.9E − 04
0.99999	223.6	897.4294	7.7E − 02	3.4E − 04

Note. Maximum and mean relative errors of the compression ratio η, $\varepsilon_r^{\max}(\eta)$ and $\bar{\varepsilon}_r(\eta)$, are given after the shock has propagated 50 zones off the wall. The zone next to the wall, which always dominates the maximum error, has not been considered when calculating the mean error.

4.2. *Relativistic Shock Tubes*

Shock tubes represent a special class of Riemann problems in which the initial state on both sides of the discontinuity is at rest. They have become a useful tool in testing numerical codes, because their evolution involves shock waves and rarefactions. We have simulated two particular shock tube problems characterized by the following initial states:

PROBLEM 1.

$$\rho_L = 10.0, \quad \rho_R = 1.0$$
$$p_L = 13.3, \quad p_R = 0$$
$$v_L = 0, \quad v_R = 0.$$

PROBLEM 2.

$$\rho_L = 1.0, \quad \rho_R = 1.0$$
$$p_L = 10^3, \quad p_R = 10^{-2}$$
$$v_L = 0, \quad v_R = 0.$$

TABLE III

L − 1 Norm Errors of Conserved Quantities and Convergence Rates Corresponding to Problem 1 at $t = 0.36$ for Relativistic PPM and Godunov's Method (Superscript G)

Δx	$\|E(D)\|_1$	$\|E(S)\|_1$	$\|E(\tau)\|_1$	r	$\|E(D)\|_1^G$	r^G
$\frac{1}{50}$	2.53E − 01	3.97E − 01	2.72E − 01		4.64E − 01	
$\frac{1}{100}$	1.43E − 01	2.54E − 01	1.67E − 01	0.82	2.89E − 01	0.68
$\frac{1}{200}$	7.51E − 02	1.19E − 01	7.80E − 02	0.93	1.84E − 01	0.65
$\frac{1}{400}$	3.98E − 02	5.77E − 02	3.83E − 02	0.92	1.14E − 01	0.69
$\frac{1}{800}$	1.94E − 02	2.96E − 02	1.93E − 02	1.04	7.03E − 02	0.70
$\frac{1}{1600}$	1.03E − 02	1.96E − 02	1.28E − 02	0.91	4.39E − 02	0.68

Note. $\|E(a)\|_1 = \sum_j \Delta x_j |a_j - A_j|$, where A_j is the exact solution at $x = x_j$.

In both cases the adiabatic index is $\gamma = 5/3$ and the initial discontinuity is placed at $x = 0.5$.

Problem 1 was chosen because it has been considered by several authors [5, 6, 14, 15], whose results can directly be compared with ours. For numerical reasons the pressure of the right state has been set to a small finite value ($p_R = 0.66 \times 10^{-6}$). The decay of the initial discontinuity gives rise to an intermediate state located between a shock wave and a rarefaction propagating to the right (i.e., positive x-direction) and left, respectively. The fluid in the intermediate state moves to the right with a velocity $v_{\text{shell}} = 0.72$. Figure 3 shows the results for a grid of 400 equidistant zones. One recognizes that the shock is smeared across 4–5 zones and that the largest errors occur for the postshock density. In Table III the errors of D, S, and τ are displayed for different grid resolutions using the discrete L-1 norm. Refining the grid the convergence rate of the solution (column 5 of Table III) indicates an order of accuracy of code of roughly 1, which is expected for problems with discontinuities and which is in good agreement with the Newtonian version of PPM [22]. This behaviour indicates that the main features of the method are retained in our relativistic version. For comparison, we have also listed in Table III the errors of the first-order accurate relativistic Godunov variant of our method. The corresponding convergence rate is only 0.66 (see Table III).

Problem 2, usually referred to as the propagation of a relativistic blast wave, was first considered by Norman and Winkler [8]. The flow pattern is similar to that of Problem 1 but somewhat more extreme. Relativistic effects reduce the postshock state to a thin dense shell. The fluid in the shell moves with $v_{\text{shell}} = 0.960$, while the shock front ahead of it (the blast wave) propagates with a velocity $v_S = 0.986$. Norman and Winkler [8] obtained very good results with an adaptive grid of 400 zones using an implicit hydro-code with artificial viscosity. Figure 4 shows the results obtained with our relativistic PPM on a fixed grid of 400 equidistant zones. As in Problem 1, the largest errors arise in the postshock state. To achieve a converged solution a grid of 2000 zones is required. Table IV gives

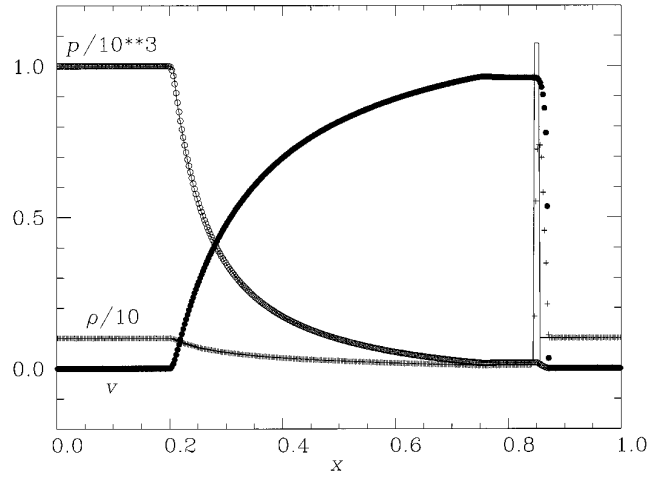

FIG. 4. Exact (solid line) and numerical profiles of pressure, density, and flow velocity of a relativistic shock tube (Problem 2; see text). The computations were performed on an equidistant grid of 400 zones.

the L-1 norm error for different grid resolutions, together with the convergence rate for both the relativistic PPM and the relativistic Godunov method.

It is worthwhile to note that in both shock tube problems, the accuracy obtained on the finest grid with the relativistic Godunov variant of our method is already achieved by the relativistic PPM with a four times coarser grid.

4.3. *Collision of Two Relativistic Blast Waves*

The collision of two strong blast waves [23] was used by Woodward and Colella [22] to compare the performance of several numerical methods (including PPM) in classical hydrodynamics. In their test calculations the initial condition consists of three constant states of an ideal gas with $\gamma = 1.4$. The density is unity and the velocity vanishes everywhere in the interval [0, 1] covered by the grid. Reflecting wall conditions are used at $x = 0$ and $x = 1$. In the left state ($x < 0.1$) the pressure $p = 10^3$, while in the right state ($x > 0.9$) $p = 10^2$

TABLE IV

L − 1 Norm Errors of Conserved Quantities and Convergence Rates Corresponding to Problem 2 at $t = 0.36$ for Relativistic PPM and Godunov's Method (Superscript G)

Δx	$\|E(D)\|_1$	$\|E(S)\|_1$	$\|E(\tau)\|_1$	r	$\|E(D)\|_1^G$	r^G
$\frac{1}{100}$	6.18E − 01	1.09E + 01	1.10E + 01		7.06E − 01	
$\frac{1}{200}$	4.94E − 01	6.61E + 00	6.43E + 00	0.32	6.38E − 01	0.15
$\frac{1}{400}$	3.21E − 01	4.25E + 00	4.10E + 00	0.62	5.45E − 01	0.23
$\frac{1}{800}$	1.78E − 01	2.71E + 00	2.67E + 00	0.85	4.63E − 01	0.24
$\frac{1}{1600}$	1.00E − 01	1.83E + 00	1.89E + 00	0.83	3.66E − 01	0.34

Note. $\|E(a)\|_1 = \sum_j \Delta x_j |a_j - A_j|$, where A_j is the exact solution at $x = x_j$.

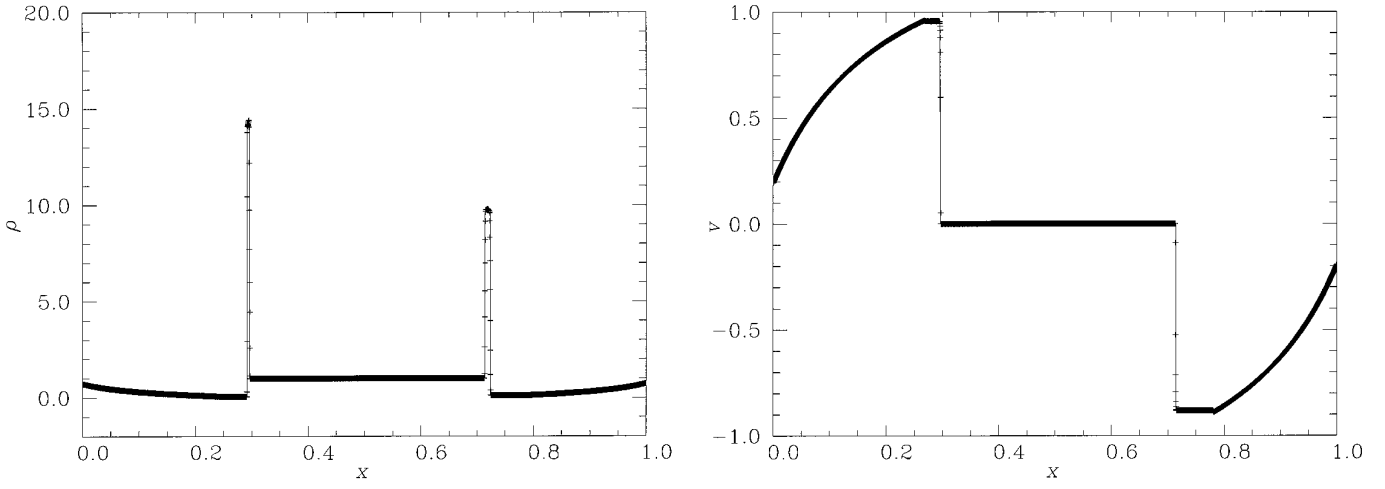

FIG. 5. (1) Exact (solid line) and numerical density profile of the colliding relativistic blast wave problem before the interaction of the waves. The computations were performed on an equidistant grid of 4000 zones. (2) Same as (1) but showing the flow velocity.

holds. In the central state ($0.1 < x < 0.9$) the initial pressure $p = 10^{-2}$.

The early evolution is characterized by the development of two strong blast waves, which propagate into the cold central gas. These waves are followed by thin shells of dense material. At $t = 0.028$, the shells collide near $x = 0.69$, resulting in a multiple interaction of strong shocks and rarefactions with each other and with contact discontinuities. Much of the wave interaction takes place in a narrow region of size $\Delta x = 0.2$. This test is considered as a very severe one, in the sense that it contains the most challenging ingredients that can appear in one-dimensional hydrodynamics, i.e., strong shocks, narrow structures, and interaction of discontinuities.

We have considered the same initial conditions to test our relativistic code. While in [22] a special version of PPM is used to produce the most accurate solution for the interaction, we have relied on the exact solution of the relativistic Riemann problem [17] to construct the analytical solution of the interacting blast wave problem. Note that this exact solution is also used in our code to calculate the numerical fluxes. Based on the exact solution of the relativistic Riemann problem, an analytical solution to the blast wave collision problem can be obtained for epochs prior to interactions with the rarefaction waves. For this reason, we have used outflow boundary conditions at $x = 0$ and $x = 1$ (to avoid the reflection and subsequent interaction of the rarefaction waves produced by the initial data) and stopped our calculations after the interaction of the leading shocks.

The evolution of the system is described in detail in Appendix II. The (dimensionless) propagation speed of the two blast waves is slower than in the Newtonian case, but very close to the speed of light (0.9776 and -0.9274 for the shock waves propagating to the right and left, respectively). Hence, the shock interaction occurs later than in the Newtonian problem, namely at $t = 0.420$. For the same reason, the dense shells are thinner, having a width at the time of the collision of $\Delta x = 0.008$ and $\Delta x = 0.019$ for the left and right shells, respectively. Consequently, the interaction is limited to an extremely narrow region of size $\Delta x \approx 0.015$. Because of the narrowness of the structures one has to use of a very fine grid to resolve the structures properly. In the calculations presented here we have used a grid of 4000 equidistant zones.

Figure 5 shows the density and velocity profiles of the flow prior to the shock collision at time $t = 0.20$. The relative error in the density of the left (right) shell never exceeds 2.0% (0.6%) and has a value of about 1.0% (0.5%) at the moment of shock collision. The quality of the numerical solution is drastically degraded when the simulations are performed with the Godunov variant of our method. At $t = 0.20$ the relative errors in the density of the left (right) shell are about 50% (16%) and drop only slightly to a value of about 40% (5%) at the time of collision ($t = 0.420$).

The collision of the shells produces a region of very high density bounded by two shocks. The density jump across the shock propagating to the left (right) is 7.26 (12.06); i.e., the value lies well above the classical limit for strong shocks (6.0 for $\gamma = 1.4$). In Fig. 6 a snapshot of the system is displayed after the interaction has occurred. Compared to Fig. 5 a largely different scale had to be used in the density plot of Fig. 6 to include the narrow dense new states produced by the interaction. Obviously, our relativistic PPM code satisfactorily resolves the structure of the collision region, the maximum relative error in the density distribution being less than 2.0%. Using the Godunov variant of our method, the new states are much more smeared out and the positions of the leading shocks are wrong (see Fig. 6).

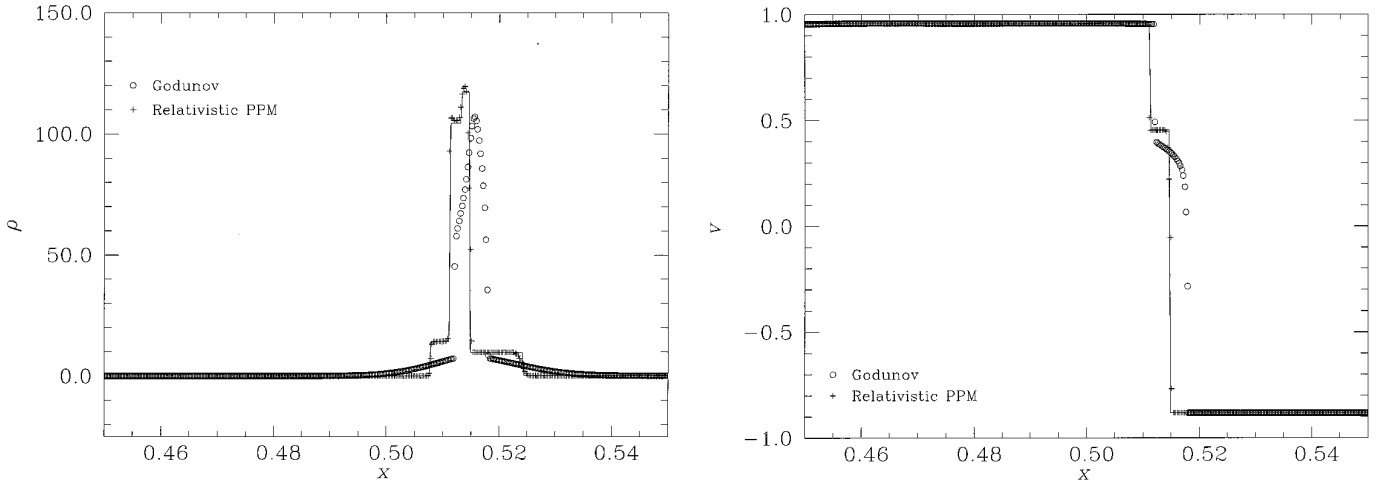

FIG. 6. (1) Same as Fig. 5(1) but after the blast wave interaction. Note the change in scale on both axes with respect to Fig. 5(1). (2) Same as Fig. 6(1) but showing the flow velocity.

5. CONCLUSIONS

We have presented and tested an extension to one-dimensional relativistic hydrodynamics of the well-known PPM method of Colella and Woodward [20]. The results obtained for problems involving ultrarelativistic flows, strong shocks, and interacting discontinuities and the comparison with Godunov's method demonstrate the superior accuracy and performance of our relativistic PPM hydrodynamics code. In the code, for the first time, an exact relativistic Riemann solver is used to compute the numerical fluxes across zone interfaces. The modular structure of the code very easily allows the incorporation of approximate relativistic Riemann solvers, too.

We also provide the exact solution of the relativistic counterpart of the collision of two blast waves [22] (see Appendix II). This solution can be used as a challenging 1D test case to calibrate relativistic hydrodynamics codes.

Finally, we mention that the method can be extended in a straightforward manner to treat also multidimensional relativistic flows. A particular multidimensional relativistic PPM code, based on an approximate relativistic Riemann solver has already been developed and successfully applied to the simulations of relativistic jets [28].

APPENDIX I: RECONSTRUCTION PROCEDURE

In this apprendix we give the details of the interpolation procedure used in our relativistic version of PPM. Although this procedure is identical to that in the original PPM formulation, we will repeat the formulae here for completeness.

Step 1. First, interpolated values of a (where a stands for any of the quantities p, ρ, v) are calculated at all zone interfaces $j + \frac{1}{2}$. These interpolated interface values $a_{j+1/2}$ are obtained using the quartic polynomial uniquely determined by the five zone-averaged values a_{j-2}, a_{j-1}, a_j, a_{j+1}, and a_{j+2}. The expression for $a_{j+1/2}$ then reads

$$\begin{aligned} a_{j+1/2} = a_j &+ \frac{\Delta x_j}{\Delta x_j + \Delta x_{j+1}}(a_{j+1} - a_j) \\ &+ \frac{1}{\sum_{k=-1}^{2} \Delta x_{j+k}} \times \left\{ \frac{2\Delta x_{j+1}\,\Delta x_j}{\Delta x_j + \Delta x_{j+1}} \right. \\ &\times \left[\frac{\Delta x_{j-1} + \Delta x_j}{2\Delta x_j + \Delta x_{j+1}} - \frac{\Delta x_{j+2} + \Delta x_{j+1}}{2\Delta x_{j+1} + \Delta x_j} \right](a_{j+1} - a_j) \\ &\left. - \Delta x_j \frac{\Delta x_{j-1}\,\Delta x_j}{2\Delta x_j + \Delta x_{j+1}}\,\delta_m a_{j+1} + \Delta x_{j+1} \frac{\Delta x_{j+1}\,\Delta x_{j+2}}{\Delta x_j + 2\Delta x_{j+1}}\,\delta_m a_j \right\} \end{aligned} \tag{59}$$

with

$$\begin{aligned} \delta_m a_j &= \min(|\delta a_j|, 2|a_j - a_{j-1}|, |a_{j+1} - a_j|)\mathrm{sign}\,(\delta a_j), \\ &\quad \text{if } (a_{j+1} - a_j)(a_j - a_{j-1}) > 0, \\ &= 0, \quad \text{otherwise}, \end{aligned} \tag{60}$$

where

$$\begin{aligned} a_j = &\frac{\Delta x_j}{\Delta x_{j-1} + \Delta x_j + \Delta x_{j+1}} \\ &\times \left[\frac{2\Delta x_{j-1} + \Delta x_j}{\Delta x_{j+1} + \Delta x_j}(a_{j+1} - a_j) + \frac{\Delta x_j + 2\Delta x_{j+1}}{\Delta x_{j-1} + \Delta x_j}(a_j - a_{j-1}) \right]. \end{aligned} \tag{61}$$

Using $\delta_m a_j$, instead of δa_j, in Eq. (60) guarantees that $a_{j+1/2}$ lies in the range of values defined by a_j and a_{j+1}. This calculation yields a value of $a_{j+1/2}$ which is third-order accurate for nonequidistant grids, even where the zone size changes discontinuously [20].

In smooth parts of the flow, away from extrema, the limiting values of a at the left and right interface, $a_{L,j} \equiv \lim_{x\to x_{j-1/2}} a(x)$ and $a_{R,j} \equiv \lim_{x\to x_{j+1/2}} a(x)$ are then given by the relation

$$a_{L,j+1} = a_{R,j} = a_{j+1/2}. \tag{62}$$

The values of $a_{L,j}$ and $a_{R,j}$ have to be modified later so that the unique parabola defined by $a_{L,j}$, $a_{R,j}$, and a_j is a monotone function in each cell, thereby introducing discontinuities at zone interfaces (see Step 4).

Step 2. The interpolation procedure described in Step 1 has to be slightly modified to produce narrower profiles in the vicinity of a contact discontinuity. This process is called contact steepening. As suggested in [20], we consider that a jump is predominantly a contact discontinuity, if the condition

$$\gamma K_0 \frac{|\rho_{j+1} - \rho_{j-1}|}{\min(\rho_{j+1}, \rho_{j-1})} \geq \frac{|p_{j+1} - p_{j-1}|}{\min(p_{j+1}, p_{j-1})} \tag{63}$$

holds, where K_0 is a constant. In all zones j satisfying (63) the density distribution is steepened by modifying the values $a_{L,j}$ and $a_{R,j}$ according to

$$\begin{aligned} a_{L,j} &\to a_{L,j}(1-\eta_j) + a^d_{L,j}\eta_j, \\ a_{R,j} &\to a_{R,j}(1-\eta_j) + a^d_{R,j}\eta_j \end{aligned} \tag{64}$$

with

$$a^d_{L,j} = a_{j-1} + \frac{\delta_m a_{j-1}}{2}, \quad a^d_{R,j} = a_{j+1} - \frac{\delta_m a_{j+1}}{2}, \tag{65}$$

and

$$\eta_j = \max[0, \min(\eta^{(1)}(\tilde{\eta}_j - \eta^{(2)}), 1)]. \tag{66}$$

In this last expression, $\eta^{(1)}$ and $\eta^{(2)}$ are free parameters, while $\tilde{\eta}_j$ is defined as

$$\tilde{\eta}_j = -\left(\frac{\delta^2 a_{j+1} - \delta^2 a_{j-1}}{x_{j+1} - x_{j-1}}\right)\left(\frac{(x_j - x_{j-1})^3 + (x_{j+1} - x_j)^3}{a_{j+1} - a_{j-1}}\right),$$

$$\text{if} \quad -\delta^2 a_{j+1}\cdot\delta^2 a_{j-1} > 0, \; |a_{j+1} - a_{j-1}| \tag{67}$$

$$-\varepsilon^{(1)}\min(|a_{j+1}|, |a_{j-1}|) > 0$$

$$= 0, \quad \text{otherwise}, \tag{68}$$

where

$$\delta^2 a_j = \frac{1}{\Delta x_{j-1} + \Delta x_j + \Delta x_{j+1}} \times \left[\frac{a_{j+1} - a_j}{\Delta x_{j+1} + \Delta x_j} - \frac{a_j - a_{j-1}}{\Delta x_j + \Delta x_{j-1}}\right]. \tag{69}$$

Step 3. Near strong shocks the order of the method is reduced locally to avoid spurious postshock oscillations. This is acheived by flattening the distribution inside the corresponding zones. In these zones the quantities $a_{L,j}$ and $a_{R,j}$ defined above are substituted by

$$\begin{aligned} a^{\text{flat}}_{L,j} &= a_j f_j + a_{L,j}(1 - f_j), \\ a^{\text{flat}}_{R,j} &= a_j f_j + a_{R,j}(1 - f_j). \end{aligned} \tag{70}$$

The weight function f_j is given by the maximum of $\tilde{f}_j$ and $\tilde{f}_{j+s_j}$, where

$$\tilde{f}_j = \min\left(1, w_j \max\left(0, \left(\frac{p_{j+1} - p_{j-1}}{p_{j+2} - p_{j-2}} - \omega^{(1)}\right)\omega^{(2)}\right)\right). \tag{71}$$

The index s_j of $\tilde{f}_{j+s_j}$ is either $+1$ or -1 depending on whether the difference $p_{j+1} - p_{j-1}$ is positive or negative. This way zone $j + s_j$ is always the next zone upstream of zone j, if the latter is in a shock.

In Eq. (71), the quotient $(p_{j+1} - p_{j-1})/(p_{j+2} - p_{j-2})$ is a measure of the steepness of the pressure jump across the zone j, $\omega^{(1)}$ and $\omega^{(2)}$ are constants, and w_j is equal to 1, if the zone is inside a shock and zero otherwise. The criterion for a zone being inside a shock is

$$\frac{|p_{j+1} - p_{j-1}|}{\min(p_{j+1}, p_{j-1})} > \varepsilon^{(2)}, \quad v_{j-1} > v_{j+1}. \tag{72}$$

Step 4. Now we are ready to describe the monotonization step (see Eq. (1.10) of [20]). In smooth parts of the flow, away from extrema, $a_{L,j+1} = a_{R,j} = a_{j+1/2}$, so that the interpolation is continuous at $x_{j+1/2}$. However, near discontinuities the values of $a_{L,j}$ and $a_{R,j}$ obtained in Step 1 to 3 are modified such that in each zone j the interpolation parabola is a monotone function, which takes on only values between $a_{L,j}$ and $a_{R,j}$. According to [20] the following modifications are necessary:

$$a_{L,j} \to a_j, \; a_{R,j} \to a_j \quad \text{if } (a_{R,j} - a_j)(a_j - a_{L,j}) \leq 0 \tag{73}$$

$$a_{L,j} \to 3a_j - 2a_{R,j} \quad \text{if } (a_{R,j} - a_{L,j}) \times \left(a_j - \frac{a_{L,j} + a_{R,j}}{2}\right) > \frac{(a_{R,j} - a_{L,j})^2}{6} \tag{74}$$

$$a_{R,j} \to 3a_j - 2a_{L,j} \quad \text{if } -(a_{R,j} - a_{L,j}) \times \left(a_j - \frac{a_{L,j} + a_{R,j}}{2}\right) > \frac{(a_{R,j} - a_{L,j})^2}{6}. \tag{75}$$

Note that in RHD the monotonic character of the reconstruction algorithmm ensures that the interpolated interface velocities are always smaller than the speed of light, if this holds for the zone averaged values, too.

The parameters K_0, $\eta^{(1)}$, $\eta^{(2)}$, and $\varepsilon^{(1)}$, introduced in Step 2,

TABLE V

Values of the Reconstruction Parameters Used in the Calculations

K_0	$\eta^{(1)}$	$\eta^{(2)}$	$\varepsilon^{(1)}$	$\omega^{(1)}$	$\omega^{(2)}$	$\varepsilon^{(2)}$
1.0	5.0	0.05	0.1	0.52	10.0	1.0

and $\omega^{(1)}$, $\omega^{(2)}$, and $\varepsilon^{(2)}$ introduced in Step 3 are, in principle, problem dependent; i.e., their values have to be fixed for every calculation. Although the quality of the results depends on the values of these parameters, a set of values can be found, however, which is well suited for a wide range of problems. The parameter values used in all our test calculations are given in Table V.

APPENDIX II: EXACT SOLUTION FOR THE COLLISION OF TWO RELATIVISTIC BLAST WAVES

In this appendix we describe the exact solution to the problem of the collision of relativistic blast waves for the initial data given in Section 4.3. The problem of the collision of two blast waves was introduced in classical hydrodynamics by Woodward and Colella [22] to test the accuracy and performance of various finite difference methods in case of a challenging numerical problem. The multiple interactions of discontinuities and rarefactions together with the resulting narrow flow structures make this problem an extremely difficult test case for any Eulerian method. In its relativistic version, we have changed the boundary conditions, however (from reflecting to outflow), to avoid the reflection and subsequent interaction of rarefaction waves. Thus, the flow structure is less complicated than in the Newtonian case. However, due to relativistic effects narrower structures and larger jumps occur in the flow.

Early on, the flow consists of two blast waves created by the decay of the initial discontinuities at $x = 0.1$ and $x = 0.9$. The two waves propagate towards each other and collide at $t = 0.4200$. We have used the procedure described in [17] to solve the Riemann problems at $x = 0.1$ and $x = 0.9$ which determine the solution before the collision. Up to this stage, the solution consists of nine different regions (R1 to R9; see Fig. 7) linked at points x_1 to x_8, where x_i is the position of the interface between regions Ri and $R(i + 1)$. Regions R1, R5, and R9 correspond to the initial states, whereas regions R3 and R4 as well as regions R6 and R7 are the intermediate states of the Riemann problem defined by the initial discontinuity at $x = 0.1$ and $x = 0.9$, respectively. The values of the hydrodynamical quantities in these constant states are given in Table VI. Finally, regions R2 and R8 are rarefaction waves.

Besides the values of the hydrodynamical quantities in the constant states, the complete analytical solution must also give the position of the points x_i ($i = 1, \ldots, 8$) as a function of time, and the flow quantities inside the rarefaction waves. Points x_1 and x_2 are the positions of the head and tail of the rarefaction wave in region R2. They move according to

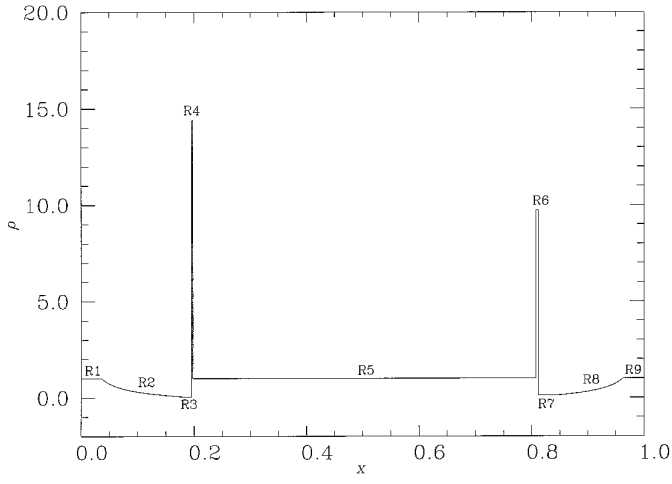

FIG. 7. Flow pattern of the colliding relativistic blast wave problem before the interaction of the waves. The values of the hydrodynamical quantities in the regions R1 to R9, which characterize the flow, are given in Table VI. They have been computed using the formulae of Appendix II.

$$x_1(t) = 0.1 - 0.6324t \tag{76}$$

$$x_2(t) = 0.1 + 0.8222t. \tag{77}$$

Inside R2, i.e., $x_1(t) < x < x_2(t)$, the distribution of the hydrodynamical quantities can be obtained in two steps. First, one solves the algebraic system of equations for the sound and flow velocity given by

$$c_2(x, t) = \frac{v_2(x, t) - (x - 0.1)/t}{1 - v_2(x, t)(x - 0.1)/t} \tag{78}$$

$$v_2(x, t) = \frac{(1 + v_1)A_+(x, t) - (1 - v_1)}{(1 + v_1)A_+(x, t) + (1 - v_1)}, \tag{79}$$

TABLE VI

Constant States of the Relativistic Blast Wave Collision Problem

Region	p	ρ	v	c
R1	1.000E + 03	1.000E + 00	0.00E + 00	6.323E − 01
R3	1.471E + 01	4.910E − 02	9.57E − 01	6.321E − 01
R4	1.471E + 01	1.439E + 01	9.57E − 01	5.591E − 01
R5	1.000E − 02	1.000E + 00	0.00E + 00	1.163E − 01
R6	4.639E + 00	9.720E + 00	−8.82E − 01	5.002E − 01
R7	4.639E + 00	1.120E − 01	−8.82E − 01	6.303E − 01
R9	1.000E + 02	1.000E + 00	0.00E + 00	6.316E − 01
C1	3.698E + 02	1.044E + 02	4.56E − 01	6.084E − 01
C2	3.698E + 02	1.173E + 02	4.56E − 01	6.056E − 01

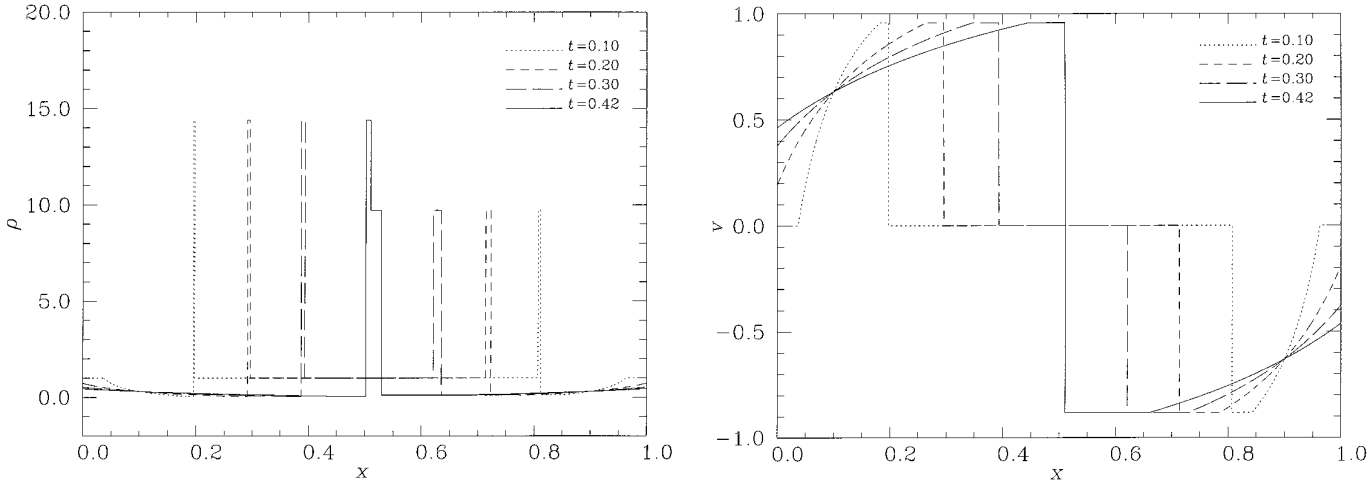

FIG. 8. (1) Sequence of snapshots showing the evolution of the density profile of the colliding relativistic blast wave problem up to the moment, when the interaction of the waves occurs. The profiles have been computed using the formulae of Appendix II. (2) Same as Fig. 8(1) but showing the flow velocity.

where

$$A_+(x,t) = \left(\frac{\sqrt{\gamma-1} - c_2(x,t)\sqrt{\gamma-1} + c_1}{\sqrt{\gamma-1} + c_2(x,t)\sqrt{\gamma-1} - c_1}\right)^{2/\sqrt{\gamma-1}}. \quad (80)$$

Then, the isentropic character of the flow inside the rarefaction can be used to get the density and pressure profiles through

$$\rho_2(x,t) = \left(\frac{c_2^2(x,t)(c_1^2-\gamma+1)}{c_1^2(c_2^2(x,t)-\gamma+1)}\right)^{1/(\gamma-1)} \rho_1 \quad (81)$$

and

$$p_2(x,t) = \left(\frac{\rho_2(x,t)}{\rho_1}\right)^{\gamma} p_1. \quad (82)$$

Point x_3 is the locus of a contact discontinuity. Hence, it moves with the velocity of the fluid in regions R3 and R4, i.e.,

$$x_3(t) = 0.1 + 0.9570t. \quad (83)$$

Point x_4, finally, gives the position of the shock heading the left blast wave propagating towards the right; i.e., its motion is governed by

$$x_4(t) = 0.1 + 0.9776t, \quad (84)$$

where the shock speed has been calculated from the Rankine–Hugoniot conditions for the jump between states R4 and R5.

The blast wave on the right has a similar structure, with a heading shock at x_5 propagating into the central initial state, a contact discontinuity at x_6 separating regions R6 and R7, and a rarefaction wave propagating to the right bounded by points x_7 and x_8. The positions of all these points as a function of time are given by

$$x_5(t) = 0.9 - 0.9274t \quad (85)$$

$$x_6(t) = 0.9 - 0.8820t \quad (86)$$

$$x_7(t) = 0.9 - 0.5668t \quad (87)$$

$$x_8(t) = 0.9 + 0.6315t. \quad (88)$$

Inside the rarefaction on the right, i.e., for $x_7(t) \le x \le x_8(t)$, the solution of the following algebraic system of equations

$$c_8(x,t) = -\frac{v_8(x,t) - (x-0.9)/t}{1 - v_8(x,t)(x-0.9)/t} \quad (89)$$

$$v_8(x,t) = \frac{(1+v_9)A_-(x,t) - (1-v_9)}{(1+v_9)A_-(x,t) + (1-v_9)} \quad (90)$$

with

$$A_-(x,t) = \left(\frac{\sqrt{\gamma-1} - c_8(x,t)}{\sqrt{\gamma-1} + c_8(x,t)}\frac{\sqrt{\gamma-1} + c_9}{\sqrt{\gamma-1} - c_9}\right)^{-2/\sqrt{\gamma-1}} \quad (91)$$

gives the sound and fluid velocity. Then, Eqs. (81) and (82) allow one to calculate $\rho_8(x,t)$ and $p_8(x,t)$, if the indices 1 and 2 are substituted by 9 and 8, respectively.

Figure 8 shows four snapshots of the evolution of the flow, including the moment of the collision of the blast waves at $t = 0.4200$. At this moment, the collision (of regions R4 and R6) occurs at $x = 0.5106$, giving rise to two new states C1

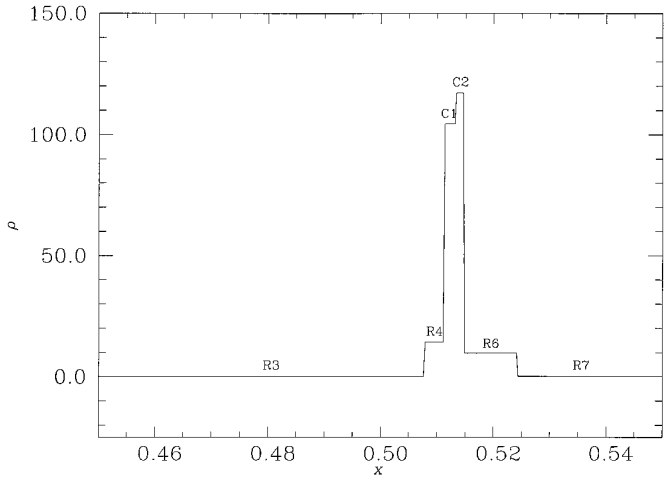

FIG. 9. Details of the density profile of the colliding relativistic blast wave problem showing the new states (regions C1 and C2; see Table VI) produced by the interaction of the two waves. Note the change in scale on both axes with respect to Fig. 8(1). The profile has been computed using the formulae of Appendix II.

and C2 (see Table VI and Fig. 9). The solution of the Riemann problem defined by the states R4 (left) and R6 (right) allows us to determine these new states, as well as the positions of the two shock waves and the contact discontinuity (x_{41}, x_{42}, and x_{43}, respectively) which separates the newly created regions from each other and from the former states R4 and R6,

$$x_{41}(t) = 0.5105 + 0.088(t - 0.4200) \tag{92}$$

$$x_{42}(t) = 0.5105 + 0.456(t - 0.4200) \tag{93}$$

$$x_{43}(t) = 0.5105 + 0.703(t - 0.4200). \tag{94}$$

The solution described above applies until $t = 0.4300$, when the next interaction (between states R4 and C1) takes place.

ACKNOWLEDGMENTS

This work has been supported by the Human Capital and Mobility Program of the Commission of the European Communities (Contract ERBCHBICT 930496). Additional financial support is acknowledged from the Spanish DGYCIT (Ref. PB91-0648). One of the authors (J.Mª.M.) would like to thank the Max-Planck-Institut für Astrophysik for the kind hospitality during his stay.

REFERENCES

1. S. Phinney, in *Superluminal Radio Sources*, edited by J. A. Zensus and T. J. Pearson (Cambridge Univ. Press, Cambridge, UK, 1987).
2. D. Strottman, in *Relativistic Fluid Dynamics*, edited by A. Anile and Y. Choquet-Bruhat (Springer-Verlag, New York/Berlin, 1989).
3. J. R. Wilson, *Astrophys. J.* **173,** 431 (1972).
4. J. R. Wilson, in *Sources of Gravitational Radiation*, edited by L. L. Smarr (Cambridge Univ. Press, Cambridge, UK, 1979).
5. J. Centrella and J. R. Wilson, *Astrophys. J. Suppl. Ser.* **54,** 229 (1984).
6. J. F. Hawley, L. L. Smarr, and J. R. Wilson, *Astrophys. J. Suppl. Ser.* **55,** 211 (1984).
7. J. von Neumann and R. D. Richtmyer, *J. Appl. Phys.* **21,** 232 (1950).
8. M. L. Norman and K.-H. A. Winkler, in *Astrophysical Radiation Hydrodynamics*, edited by M. L. Norman and K.-H. A. Winkler (Reidel, Dordrecht, 1986).
9. J. Mª. Martí, J. Mª. Ibáñez, J. A. Miralles, *Phys. Rev*. **D 43,** 3794 (1991).
10. M. R. Dubal, *Comput. Phys. Commun.* **64,** 221 (1991).
11. P. J. Mann, *Comput. Phys. Commun.* **67,** 245 (1991).
12. A. Marquina, J. Mª. Martí, J. Mª. Ibáñez, J. A. Miralles, and R. Donat, *Astron. Astrophys.* **258,** 566 (1992).
13. M. H. P. M. van Putten, *J. Comput. Phys.* **105,** 339 (1993).
14. V. Schneider, U. Katscher, D. H. Rischke, B. Waldhauser, J. A. Maruhn, and C.-D. Munz, *J. Comput. Phys.* **105,** 92 (1993).
15. F. Eulderink, Ph.D. thesis, Rijksuniversiteit te Leiden, 1993 (unpublished).
16. R. J. LeVeque, *Numerical Methods for Conservation Laws* (Birkhäuser, Basel, 1992).
17. J. Mª. Martí and E. Müller, *J. Fluid Mech.* **258,** 317 (1994).
18. K. W. Thompson, *J. Fluid Mech.* **171,** 365 (1986).
19. B. J. Plohr and D. H. Sharp, in *The VIIIth International Conference on Mathematical Physics*, edited by M. Mebkhout and R. Sénéor (World Scientific, Singapore, 1987).
20. P. Colella and P. R. Woodward, *J. Comput. Phys.* **54,** 174 (1984).
21. S. K. Godunov, *Mat. Sb.* **47,** 271 (1959).
22. P. R. Woodward and P. Colella, *J. Comput. Phys.* **54,** 115 (1984).
23. P. R. Woodward, in *Parallel Computation*, edited by G. Rodrigue, (Academic Press, New York/London, 1982).
24. R. Courant and K. O. Friedrichs, *Supersonic Flow and Shock Waves* (Springer-Verlag, New York/Berlin, 1976).
25. G. E. Forsythe, M. A. Malcolm, and C. B. Moler, *Computer Methods for Mathematical Computations* (Prentice–Hall, Englewood Cliffs, NJ, 1977).
26. P. Colella and H. M. Glaz, *J. Comput. Phys.* **59,** 264 (1985).
27. T. L. McAbee, J. R. Wilson, J. A. Zingman, and C. T. Alonso, *Mod. Phys. Lett. A* **4,** 983 (1989).
28. J. Mª. Martí, E. Müller, and J. Mª. Ibáñez, *Astron. Astrophys.* **281,** L9 (1994).